

UNDERSTANDING THE PATH TO CONTACT SILICON SOLAR CELLS WITH
140 Ω/sq HIGH RESISTANCE EMITTERS

by

Keming Ren

A thesis submitted to the faculty of
The University of North Carolina at Charlotte
in partial fulfillment of the requirements
for the degree of Master of Science in
Electrical Engineering

Charlotte

2019

Approved by:

Dr. Abasifreke Ebong

Dr. Yong Zhang

Dr. Ed Stokes

©2019
Keming Ren
ALL RIGHTS RESERVED

ABSTRACT

KEMING REN. Understanding the Path to Contact Silicon Solar Cells with
140 Ω/sq High Resistance Emitters.

(Under the direction of DR. ABASIFREKE EBONG)

Solar cell electricity can only be attractive if it is cost effective. In order for it to be affordable, the cost of manufacturing the solar cell must be decreased. Both material use and improved efficiency should be addressed in order to realize this goal. One of the paths to improve efficiency is to fabricate the cells on lowly doped emitters, which is difficult to contact with the present screen-printing technology. In this thesis work, the study of the microstructure of the *Ag* gridline/*Si* interface was carried out to elucidate the elemental composition of the glass layer underneath this contact. SEM, EDS and Raman Spectrometer were used to analyze two cells (one each) made with two different paste samples. The SEM showed that the worse cell had very thick glass layer underneath the metal contact. This cell also showed very high contact resistance and low fill factor (*FF*). Upon the removal of the metal contact and the glass layer, the *Ag* crystallites in the *Si* emitter were less compared to the better cell with low contact resistance and high *FF*. The EDS confirmed that the existence of *Al*, *Pb*, *Te*, *Ag* and *Bi* in the glass but not in the *Si* emitter. This was confirmed by the Raman spectra with the peaks that aligned with some compounds of *Pb* and *Te*. This showed that the glass layer contains some alloys of *Pb* and *Te* and these alloys tend to increase its conductivity and decrease the contact resistance. It can therefore be inferred that, the glass layer increased conductivity in conjunction with the *Ag* crystallites embedded in *Si* emitter will lead to an optimized contact on the lowly doped emitter.

ACKNOWLEDGEMENTS

First and foremost, I would like to thank the Nanoscale Science program in Chemistry Department at UNC Charlotte for supporting my M.S. Degree in the Electrical and Computer Engineering. Everything happened during my M.S., taking courses and doing research, is very memorable and enjoyable.

Secondly, I would also like to thank my supervisor Prof. Dr. Abasifreke Ebong of Electrical and Computer Engineering. He is a nice, experienced and farsighted professor who advises me in the right direction and guide me step by step.

In addition, I would like to thank Dr. Yong Zhang and Dr. Ed Stokes for taking the time to serve on my thesis committee.

Finally, I would express my profound gratitude to my families for providing me with spiritual support and continuous encouragement.

TABLE OF CONTENTS

LIST OF FIGURES	vi
LIST OF TABLES	viii
LIST OF ABBREVIATIONS	1
CHAPTER 1: INTRODUCTION	1
CHAPTER 2: SOLAR CELL WORKING PRINCIPLES	7
2.1. Silicon Solar Cell Structure	7
2.2. The Output Parameters of a Solar Cell	9
2.3. Types of Commercial Solar Cells	14
2.4. Fabrication of a Solar Cell	15
CHAPTER 3: DESIGN AND MODELING OF A HIGH EFFICIENT COMMERCIAL SOLAR CELL	18
CHAPTER 4: EXPERIMENTAL	26
4.1. Electrical Analyses	27
4.2. Micro-Structure Analyses	27
4.2.1. SEM and EDS	27
4.2.2. Raman Study	32
CHAPTER 5: CONCLUSIONS	34
CHAPTER 6: FUTURE WORK	35
REFERENCES	36

LIST OF FIGURES

FIGURE 1.1: Global surface temperatuer anomalies.	1
FIGURE 1.2: Energy related carbon dioxide emissions.	2
FIGURE 1.3: World energy consumption from 2012 to 2040.	3
FIGURE 1.4: Annual electricity generating capacity.	4
FIGURE 1.5: Renewable electricity generation.	4
FIGURE 1.6: Buildings sector on-site electric generating capacity.	5
FIGURE 2.1: $n - type$ and $p - type$ regions are both created on one substrate.	8
FIGURE 2.2: Build-in electric field.	8
FIGURE 2.3: Conventional c- <i>Si</i> solar cell operation.	9
FIGURE 2.4: Equivalent circuit of a one-diode model of a slar cell under ideal condition (with illumination).	10
FIGURE 2.5: Equivalent circuit of a two-diode model solar cell under non-ideal condition (with illumination).	11
FIGURE 2.6: The Graph of the I-V characteristics of an ideal diode solar cell in the dark and under illumination.	13
FIGURE 2.7: Scheme of Al-BSF cell	15
FIGURE 2.8: Scheme of PERC cell	15
FIGURE 2.9: Manufacture of screen-printed Al-BSF solar cell from Si wafer	17
FIGURE 3.1: PC1D modeling device schematic.	19
FIGURE 3.2: Impact of R_s on the (a) V_{oc} , (b) J_{sc} , (c) FF and (d) Efficiency under different FR.	22
FIGURE 3.3: Components of series resistance in soalr cells.	23

FIGURE 3.4: The relationship between surface doping concentration and the emitter resistivity.	24
FIGURE 3.5: Impact of N_s on the (a) V_{oc} and J_{sc} , (b) FF and Efficiency.	24
FIGURE 4.1: SEM cross-section images of A, (a-b) before acid treatment, (c-d) after Ag gridline removal; (e-f) after interface glass removal.	28
FIGURE 4.2: SEM cross-section images of sample D, (a-b) before acid treatment, (c-d) after Ag gridline removal; (e-f) after interface glass removal.	30
FIGURE 4.3: EDS analyses of selected area on sample D (a) after Ag gridline removal; (b) after interface glass removal.	32
FIGURE 4.4: Raman spectroscopy of sample A, D after HNO_3 and HF treatment and Ag_2Te , $PbTe$.	33

LIST OF TABLES

TABLE 3.1: PC1D modeling: device initial parameters	20
TABLE 4.1: Electrical properties of the four samples made by different pastes.	27

CHAPTER 1: INTRODUCTION

Global warming is the climate change in the earth's climate system due to the emission of greenhouse gases, such as CO_2 , CH_4 , and N_2O . Figure 1.1, shows that, since in the 1900s, the global mean surface temperature has been raised by $1.4\text{ }^\circ C$. The side effects of the global warming have shown: (1) increase in extreme weather with greater warming and change in precipitation over land areas; (2) rising sea level around 2.7 mm per year since 1993 and from 1995 to 2015, with accelerating raising speed [1]; and (3) effect on ecological systems and extinction of some species. To reduce the global warming and stabilize the global average, the emission of CO_2 must be reduced as well as other greenhouse gases.

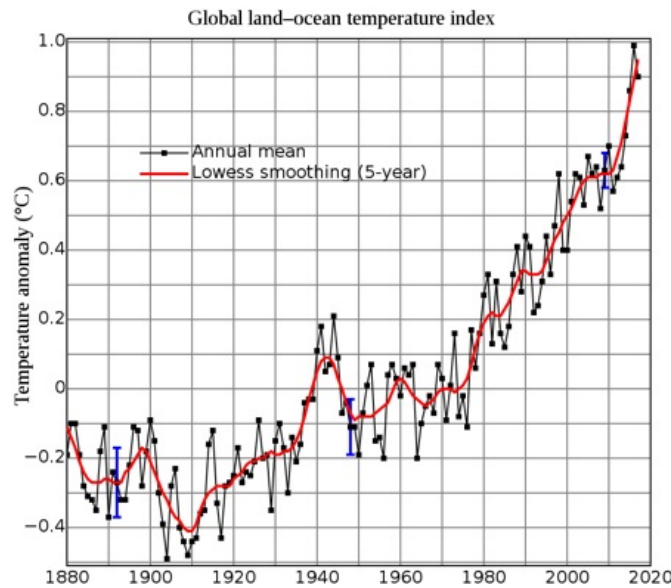


Figure 1.1: Global surface temperature anomalies relative to 1951-1980 mean for annual and 5 years running means through 2017 [2].

However, according to the international energy outlook 2017 published by U.S. Energy Information Administration [3], the CO_2 emissions caused by coal increased

at an average rate of 2.3%/year from 1990 to 2015, and after 2015, it still increased at rate of 0.1% (Figure 1.2). The liquids-related CO_2 emissions increased by an average of 1.2%/year from 1990 to 2015 and will continue to increase by average of 0.7%/year from 2015 to 2040. The CO_2 emissions from natural gas grow by an average of 2.2%/year from 1990 to 2015 and will be reduced to 1.4%/year by 2015 and 2040. However, even though after 2015, the average speed of CO_2 emissions is reduced, the total tons of CO_2 will still be at a high level.

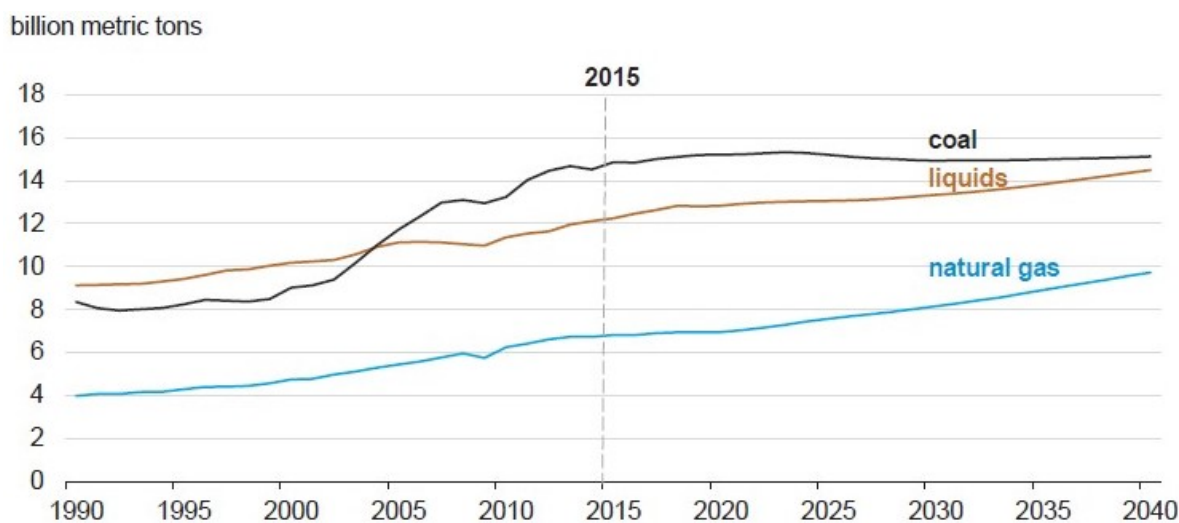


Figure 1.2: Energy related carbon dioxide emissions.

Figure 1.3 shows the International Energy Outlook for 2016 [4], the worldwide energy demand from 2012 to 2040 with significant growth from 549 quadrillion British thermal units (Btu) in 2012 to 815 quadrillion Btu in 2040 at an average rate of 1.4%/year. A total of 48% energy consumption increase in 2040 will require extra half energy source to be exploited. In order to achieve both world energy demand and global environment protection, we must develop clean energy, such as solar, wind, and geothermal, without further delay.

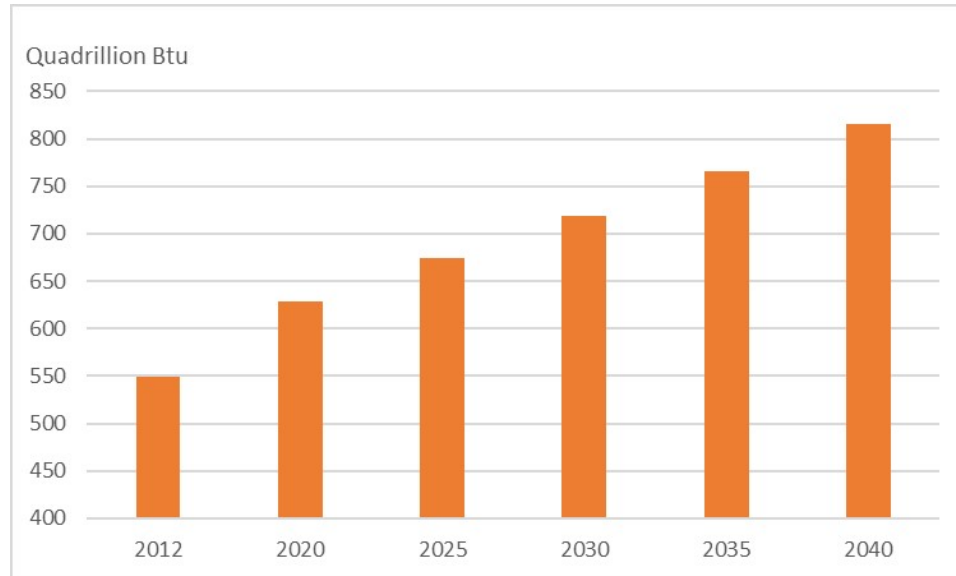


Figure 1.3: World energy consumption from 2012 to 2040.

Due to unlimited energy source from the sun, solar energy can be the promise of clean and decentralized energy for the whole world. Developing new energy converting technologies and at the same time retiring low efficient and high-pollution energy generation units are the important contents during energy revolution. According to the Annual Energy Outlook 2017 by U.S. Energy Information Administration [5], the retired older and less efficient fossil fuel units, including coal, oil, and gas, have been replaced by wind and solar plants since 2005 as shown in Figure 1.4.

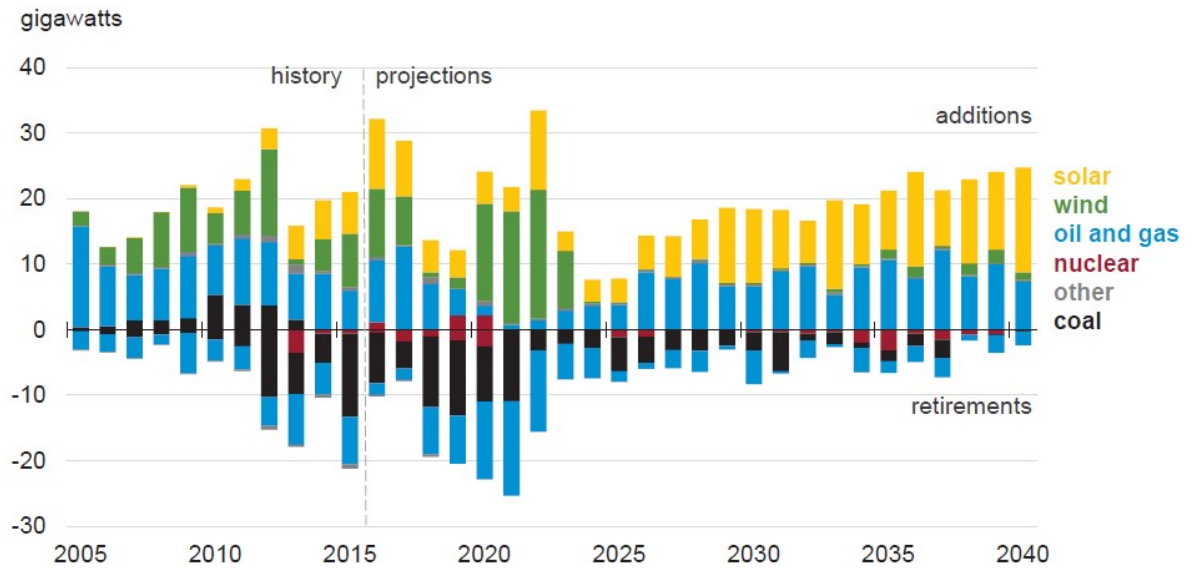


Figure 1.4: Annual electricity generating capacity additions and retirements.

Throughout the projection period, the older, less efficient fossil fuel units will continue to be retired and replaced by new generating capacity. After 2030, solar capacity will be around 50% of the new generation capacity and it will be close to the amount of natural gas. In Figure 1.5, after 2016, the wind and solar electricity generation have been the two main growing parts among the whole renewable electricity generation.

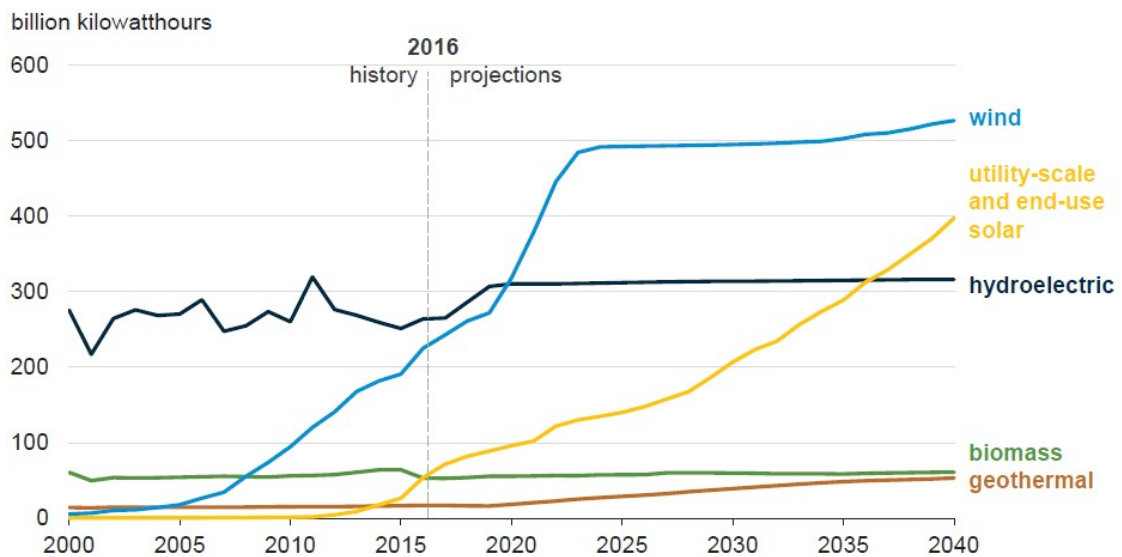


Figure 1.5: Renewable electricity generation.

After 2025, solar electricity generation will still be growing and could double in 2040. The most growth of solar photovoltaic systems will be in the building sector, the on-site electric generation as predicted in Figure 1.6. According to the prediction by the energy outlook, the total solar generation capacity growth, which started in 2010 at less than 2 gigawatts will reach 125 gigawatts in 2040. All other technologies in the commercial sector, including combined heat and power, will slowly reach 13 gigawatts by 2040.

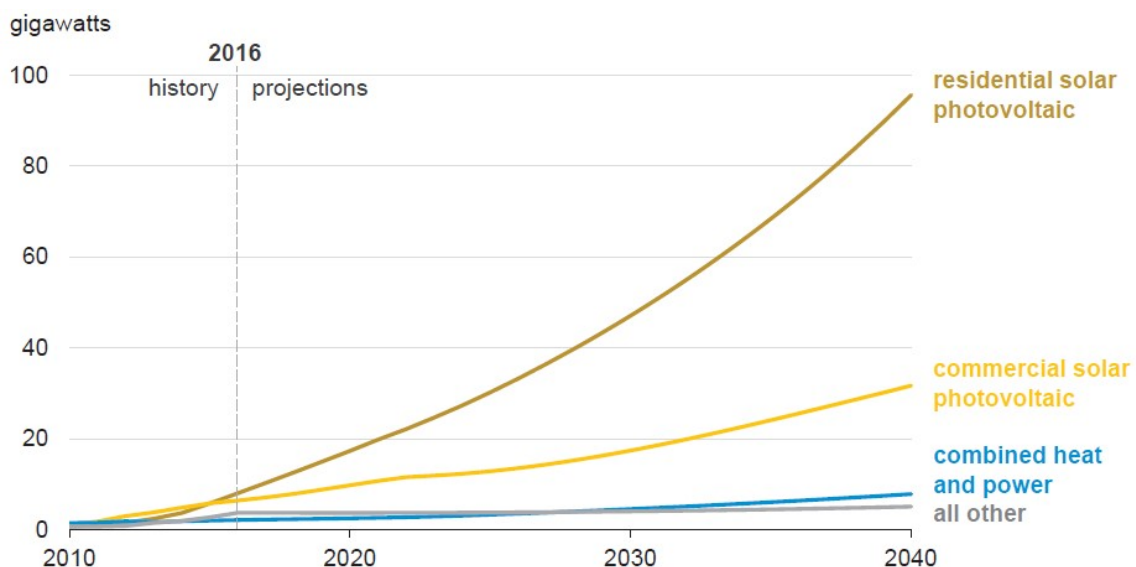


Figure 1.6: Buildings sector on-site electric generating capacity.

In order to achieve the goal of 2040, the cost of solar cells must be reduced with increasing efficiency. However, to fabricate cost effective solar cells with high efficiency, understanding every layer of the solar cell structure is needed. For instance, the efficiency of a solar cell is dependent on the peak surface doping concentration (N_s) of the emitter because the emitter with lower N_s makes the cell more transparent to photons with less surface charge recombination. But, such emitter is difficult to contact with the commercial screen-printing technology. Thus, the microstructure analyses of the contact is needed to fully evaluate the Ag/Si interface to identify the elements and alloys (if any) present in the glass layer and their interaction with

the Ag crystallites embedded in silicon after the contact formation step. Based on this understanding that the lowly doped emitter ($140\Omega/sq$) can be contacted with low contact resistance to achieve high FF and hence efficiency in excess of 26% [6] without any added cost. This lines up well with report by International Technology Roadmap for Photovoltaic (ITRPV) in 2018 [7]. This thesis work therefore, serves as a case study to understand the path to contact lowly doped emitter with low contact and gridline resistances.

CHAPTER 2: SOLAR CELL WORKING PRINCIPLES

2.1 Silicon Solar Cell Structure

The working principle of a solar cell, which was discovered by a French physicist Alexandre Edmond Becquerel in 1839, is based on photovoltaic effect, where light can be converted into electricity. In 1954 [8], the first solar cell was created on a diffused $p - n$ junction by Bell Labs. After more than 60 years, photovoltaic technology has been developed rapidly, but currently most commercial solar cells are still based on the $p - n$ junction structure.

The $p - n$ junction is a junction between an $n - type$ semiconductor and a $p - type$ semiconductor. An $n - type$ semiconductor is a semiconductor material doped with donor impurities, to increase electrons in the conduction band and a $p - type$ semiconductor is doped with acceptors to create holes in valence band, as shown in Figure 2.1. As a result, there are many electrons and less holes in the $n - type$ material and the majority carriers in the $p - type$ material are holes and the minority are electrons. When $n - dopants$ are diffused into a $p - type$ substrate, an $n - type$ region (up to $0.2 - 0.5\mu m$ thick) is created. Once there are both $n -$ and $p - type$ regions created on one substrate, electrons will diffuse from the $n - type$ material to the $p - type$ material and at the same time, holes will diffuse from the $p -$ side to the $n -$ side. When negative electrons diffuse from the $n -$ side across toward the $p -$ side, positive charges will be left behind. Similarly, positive holes diffuse from the $p -$ side across toward the $n -$ side, negative charges will be left behind. These fixed charges form an electric field exactly at the junction between the $n -$ and $p -$ materials, called built-in electric field in Figure 2.2 [9]. This built-in electric field will force charges to

move in the opposite direction of the diffusion and finally reach a stable equilibrium, where the net flow of electrons and holes through the junction is zero.

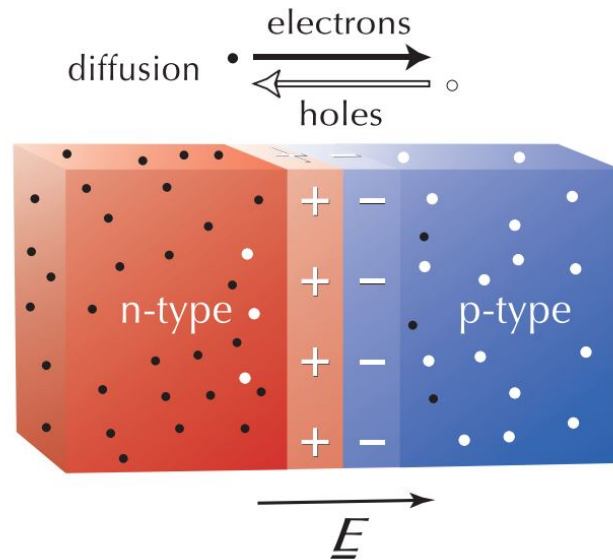


Figure 2.1: *n* – *type* and *p* – *type* regions are both created on one substrate [9].

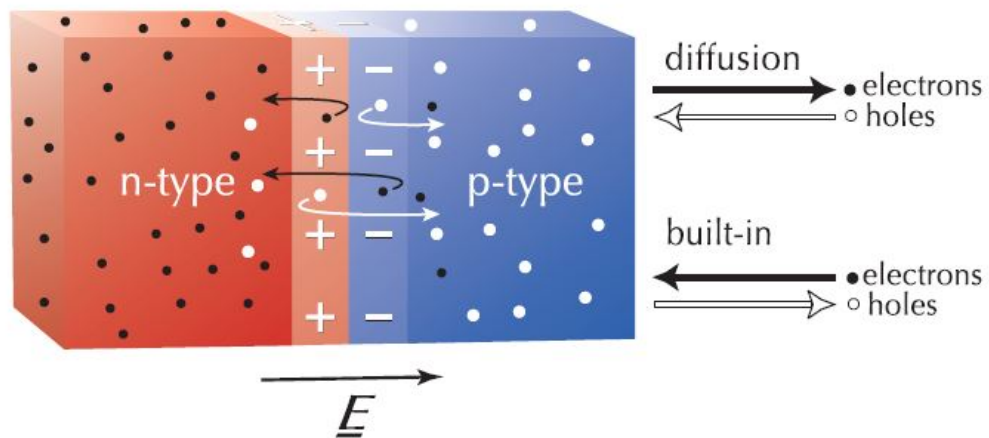


Figure 2.2: Build-in electric field [9].

The simplest *p* – *n* junction solar cell is shown in Figure 2.3, where silicon wafer is doped to have an *n*– and *p*– regions. On the front surface of the *n*– region, there are front metal contacts and meanwhile the rear side at the *p*–*type* region is covered by a rear metal contact. When the light shines on the front side of the solar cell, the

light with higher energy than the band gap of Si is absorbed by the solar cell and then electron-hole pairs are generated. It is possible that the generated electron-hole pairs will recombine with each other and no current will be produced. But due to the existence of a built-in electric field in the $p - n$ junction, the electron-hole pair generated near the $p - n$ junction will be forced to separate and under the electric field, the electrons move to the n - side and holes reach the p - side. As a result, because of the separation of electrons and holes, the collection efficiency of charge carriers is highly increased. Once diffused to the edge of the cell, the electrons and holes can be collected and provide electricity to the load.

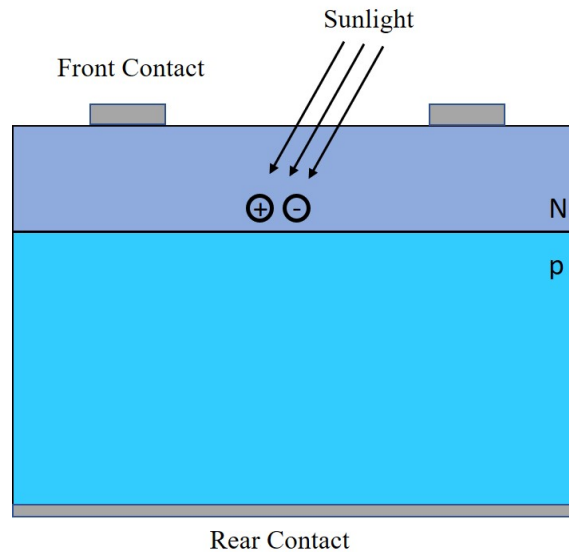


Figure 2.3: Conventional c - Si solar cell operation [10].

2.2 The Output Parameters of a Solar Cell

The equivalent circuit of a solar cell under ideal condition is shown in Figure 2.4.

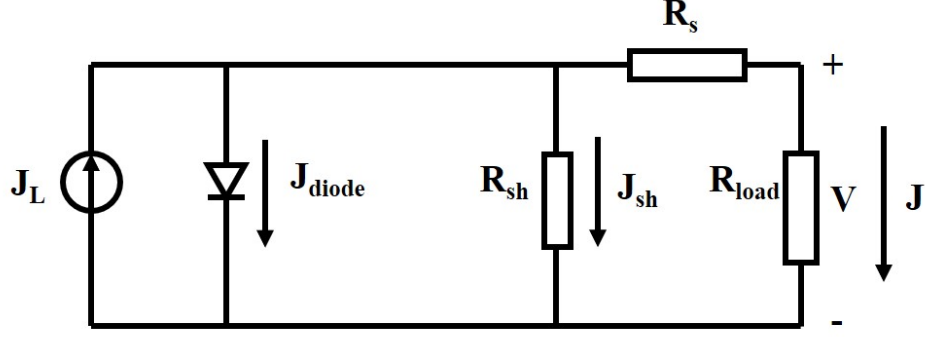


Figure 2.4: Equivalent circuit of a one-diode model of a solar cell under ideal condition (with illumination).

where J_L is the photocurrent density, J_{diode} is the ideal diode current density, R_{sh} is the shunt resistance, J_{sh} is the shunt current density through R_{sh} , R_s is the series resistance, R_{load} is the load resistance and J is the output current density. Under ideal conditions, R_{sh} is assumed to be very large to ensure that J_{sh} is zero and R_s is assumed to be very small ($< 0.1 \Omega.cm^2$). The output current density J and ideal diode current density J_{diode} were shown in Equations 2.1 and 2.2.

$$J = J_L - J_{diode} \quad (2.1)$$

$$J = J_L - J_o \left(\exp \frac{qV}{nkT} - 1 \right) \quad (2.2)$$

where J_o is the reverse-biased saturation current density, q is the electron charge, k is the Boltzmann constant, T is the temperature and n is the ideality factor (where $n = 1$ for an ideal diode and $n > 1$ for a non-ideal diode).

However, the diode is mostly working under a non-ideal situation because of charge recombination.

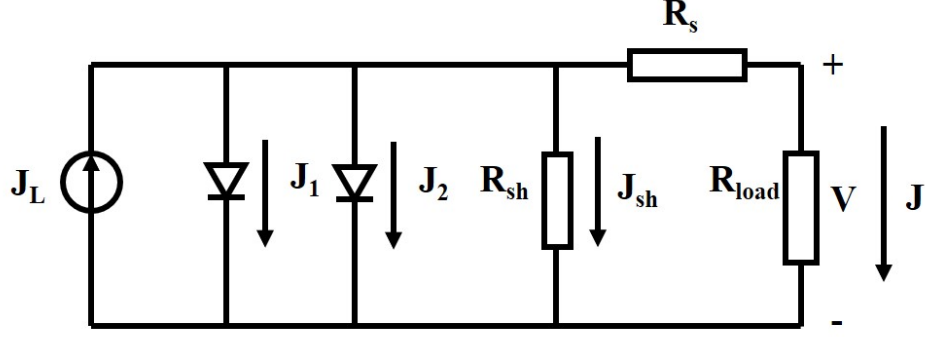


Figure 2.5: Equivalent circuit of a two-diode model solar cell under non-ideal condition (with illumination).

Figure 2.5 shows the two diode model of a solar cell taking account of the junction recombination, where J_1 is the diode current and J_2 is the recombination current density. In this case, the total current density J is given by Equation 2.3 and 2.4.

$$J = J_L - (J_1 + J_2 + J_{sh}) \quad (2.3)$$

$$J = J_L - \left\{ J_{o1} \left(\exp \frac{q(V + JR_s)}{n_1 kT} - 1 \right) + J_{o2} \left(\exp \frac{q(V + JR_s)}{n_2 kT} - 1 \right) + \frac{V + JR_s}{R_{sh}} \right\} \quad (2.4)$$

where J_{o1} is a reverse-biased saturation current density and J_{o2} is the recombination current density. n_1 and n_2 are the ideality factors. To have a good performance solar cell, R_s should be minimized, R_{sh} should be maximized and J_{o2} should be minimized.

In the analysis of the performance of a solar cell, the circuit is considered under two situations, short circuit and open circuit. At short circuit, the photocurrent generated by a solar cell under illumination is short-circuit current (I_{sc}) where R_s and R_{load} are both zero. The short-current density (J_{sc}) is given by the Equation 2.5.

$$J_{sc} = J_L - \left\{ J_{o1} \left(\exp \frac{qV}{n_1 kT} - 1 \right) + J_{o2} \left(\exp \frac{qV}{n_2 kT} - 1 \right) \right\} \quad (2.5)$$

At open circuit, when the R_{load} and R_s are infinitely large, the potential difference between the terminals of the cell is called open-circuit voltage (V_{oc}), shown in Equation 2.6, where J_{oe} is the emitter saturation current density and J_{ob} is the base

saturation current density.

$$V_{oc} = \frac{nkT}{q} \ln \left(\frac{J_L}{J_o} + 1 \right) = \frac{nkT}{q} \ln \left(\frac{J_L}{J_{oe} + J_{ob}} + 1 \right) \quad (2.6)$$

when assuming $J_L = J_{sc}$,

$$V_{oc} = \frac{nkT}{q} \ln \left(\frac{J_{sc}}{J_{oe} + J_{ob}} + 1 \right) \quad (2.7)$$

then [11]

$$J_{oe} = F_m J_{oem} + (1 - F_m) J_{oeSiN} \quad (2.8)$$

$$J_{ob} = \frac{qn_i^2}{N_A} \frac{D}{L_{eff}} \quad (2.9)$$

$$J_{o1} = J_{oe} + J_{ob} \quad (2.10)$$

where F_m is the solar gridline coverage fraction, J_{oem} is the emitter saturation current density under metal gridline, J_{oeSiN} is the saturation current of the passivated layer, n_i is the intrinsic carrier density of the material, N_A is the acceptor carrier density, D is the diffusivity of minority carrier, L_{eff} is the effective minority carrier diffusion length [12].

Based on J. Nelson [13], the J_{sc} can also be expressed by quantum efficiency (QE) which is the probability that an incident photon of energy (E) will generate one electron to the external circuit. It depends on the the absorption coefficient of the material, the efficiency of charge separation, the efficiency of charge collection, and the incident light energy. The photocurrent density (J_{sc}) can be expressed by the following equation:

$$J_{sc} = q \int b_s(E) QE(E) dE \quad (2.11)$$

where $b_s(E)$ is the incident spectral photon flux density, the number of photons of energy in the range from E to $E + dE$ which are the incident on unit area in unit time and q is the electronic charge. QE is an important factor to describe solar cell performance under different conditions. There are two types of quantum efficiency of solar cells: External Quantum Efficiency (EQE) and Internal quantum efficiency

(*IQE*). The *EQE* is the ratio of the number of charge carriers collected by the solar cell to the number of photons of a give energy shining on the solar cell. The *IQE* is the ratio of the number of charge carriers collected by the solar cell to the number of photons of a given energy that is absorbed by the cell [14].

When a voltage or bias V is applied between terminals of the cell in the dark, there will be a current flow across the device, which is usually called the dark current $I_{dark}(V)$, and much larger current flows across the device under forward bias ($V > 0$) than under reverse bias ($V < 0$), as shown in Figure 2.6 [15]. For an ideal diode, the dark current density $J_{dark}(V)$ is

$$J_{dark}(V) = J_o(e^{qV/k_B T} - 1) \quad (2.12)$$

Where J_o is a constant, k_B is Boltzmann's constant and T is temperature in degrees Kelvin. The net current density in the cell is:

$$J(V) = J_{sc} - J_{dark}(V) \quad (2.13)$$

which becomes, for an ideal diode

$$J = J_{sc} - J_o(e^{qV/k_B T} - 1) \quad (2.14)$$

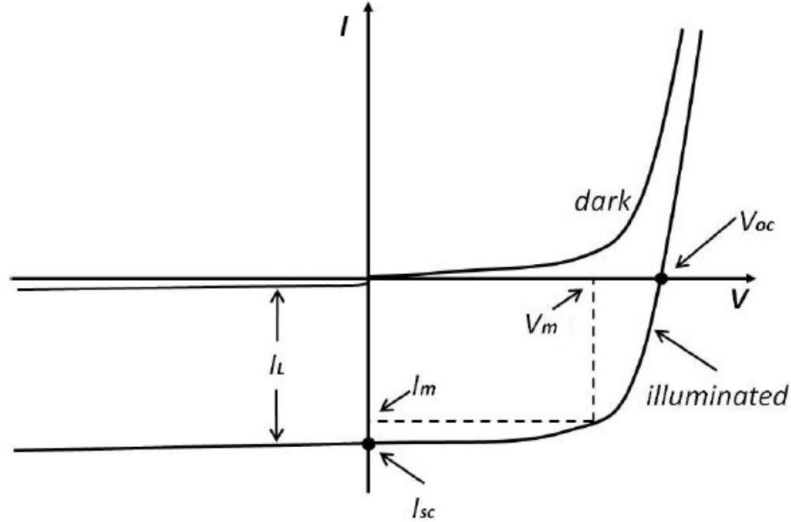


Figure 2.6: The Graph of the I-V characteristics of an ideal diode solar cell in the dark and under illumination [15].

The solar cell power density(P) is given by:

$$P = JV \quad (2.15)$$

And P reaches a maximum power point P_m at V_m and J_m , where $P_m = J_m V_m$. The fill factor (FF) is the ratio of maximum obtainable power (P_m) to the product of J_{sc} and V_{oc} :

$$FF = \frac{J_m V_m}{J_{sc} V_{oc}} \quad (2.16)$$

The efficiency (η) of the solar cell is the power density delivered at the operating points as a fraction of the incident light power density (P_s):

$$\eta = \frac{J_m V_m}{P_s} \quad (2.17)$$

related to J_{sc} , V_{oc} and FF ,

$$\eta = \frac{J_{sc} V_{oc} FF}{P_s} \quad (2.18)$$

2.3 Types of Commercial Solar Cells

The crystalline silicon solar cell, including the polycrystalline and monocrystalline, has had about 90% global photovoltaic market share and the highest efficient Si solar cell has reached 26.6 % efficiency according to Kaneka [16]. The screen-printed aluminum back surface field (Al-BSF) $p - type$ solar cell has an efficiency raised to 20.29%[17]. The structure of Al-BSF is shown in Figure 2.7, where from top to bottom, the textured front surface and the SiN_x layer are both aimed to reduce light reflection. Below SiN_x , the wafer is doped with phosphorus to be $n - type$ and the bulk is $p - type$ doped with boron. The front and rear metal contacts are silver and aluminum, respectively, formed by screen-printing metal pastes onto the wafer and fired under high temperature. Based on the structure of Al-BSF, passivated emitter and rear cell (PERC) has been developed, Figure 2.8. Compared to Al-BSF cell, the main difference is that the back contact of the PERC cell is only a fraction of the back side with the rest area being passivated with Al_2O_3/SiN_x . As a result, the back surface recombination is highly reduced to achieve higher V_{oc} and the highest

efficiency for PERC cell is 22.61% [18]. Both Al-BSF and PERC cells are the two major types of commercial solar cells and the front contacts of both cells are fabricated by screen-printing technology.

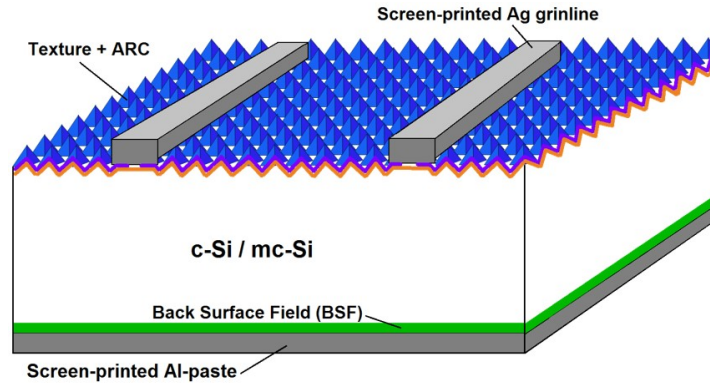


Figure 2.7: Scheme of Al-BSF cell.

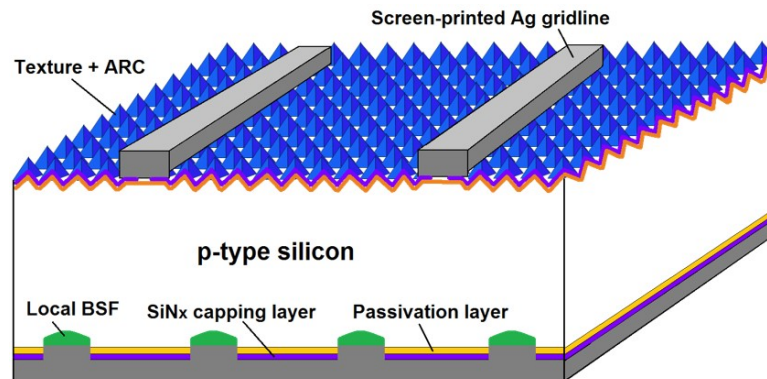


Figure 2.8: Scheme of PERC cell.

2.4 Fabrication of a Solar Cell

The commercial solar cell is fabricated on *Si* wafers, which are made from polysilicon. The polysilicon is manufactured by firing sand (silica) with coke in an arc furnace at 1800°C followed by chemical refinement (HCl , H_2). After that, Czochralski process is used to grown mono crystalline Si where the polysilicon is melted in a crucible at 1424°C first. Dopant impurity atoms such as boron or phosphorus can be added into the melted silicon to make *p*- or *n*-type silicon. Then a precisely oriented rod-mounted seed crystal is dipped into the molten silicon. By controlling

the temperature gradients and the rate of pulling and rotating the seed crystal, it can grow a large, single-crystal ingot. Finally, the wafers are made by using diamond saw to slice the *Si* crystal ingot.

Figure 2.9 outlines the fabrication process for a *p*-based crystalline Si solar cell which includes: (1) saw damage removal by alkaline or acidic solutions as well as plasma etching and at the same time forming a surface texture to reduce the surface reflection, followed by wafer cleaning in deionized water; (2) phosphorous diffusion to form *n-type* region by using $POCl_3$ at $800 \sim 900^\circ C$; (3) phosphorus glass removal in *HF* solution and rear side texture in acid solution to isolate the front and rear sides; (4) antireflection coating by plasma-enhanced chemical vapor deposition (PECVD); (5) screen printing the front silver contacts and back aluminum contacts by squeegee moving with a defined pressure to push the *Ag* and *Al* pastes through the screen and print onto the wafer; (6) cofiring the *Ag* and *Al* contacts around $800^\circ C$ for a short time; (7) the light-current-voltage (LIV) measurement.

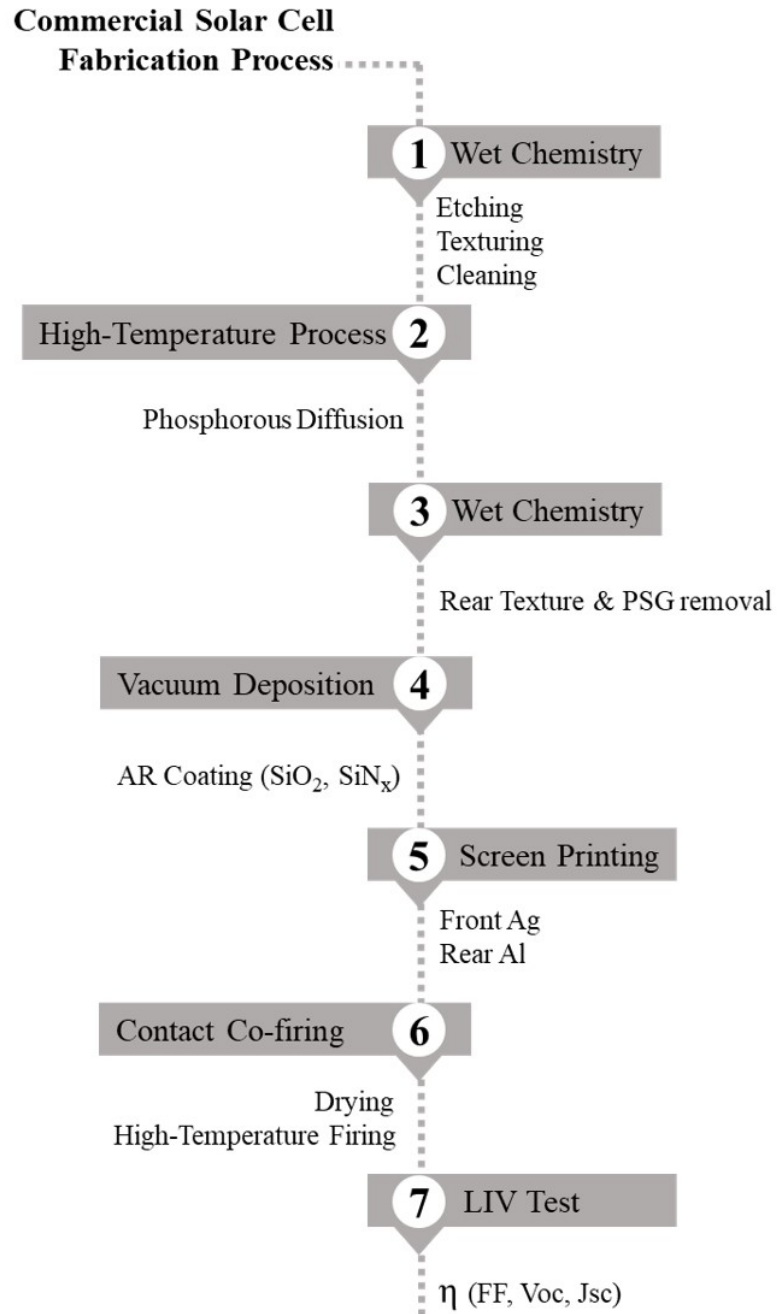


Figure 2.9: Manufacture of screen-printed Al-BSF solar cell from Si wafer.

CHAPTER 3: DESIGN AND MODELING OF A HIGH EFFICIENT COMMERCIAL SOLAR CELL

Since a solar cell is an opto-electronic device, both optical and electrical losses must be minimized in order to fabricate a highly efficient solar cell. The objective of this thesis work is to identify both sources, the optical and electrical losses, related to the layers of a solar cell through modeling. The design of the solar cell is using a one-dimensional computer program (PC1D) [19], which numerically solves the fully coupled nonlinear equations for the quasi-one-dimensional transport of electrons and holes in crystalline semiconductor devices. Pertinent to the losses are: (i) the surface reflectance encompassing the antireflective coating, gridlines and busbar shadowing which pertains to optical losses; (ii) surface passivation, which controls the surface recombination (electrical losses); and (iii) series resistance, which impacts the maximum power output of any solar cell. The best solar cell should have very low total front surface reflectance to allow high photon absorption; low surface and bulk recombination to allow the created electron-hole pairs to be separated and collected for high short circuit current; high open circuit voltage; and the contacts should not exhibit $I^2 \cdot R$ power loss. The typical PC1D device schematic is shown in Figure 3.1, which is just a one-diode model with shunt resistance across the p-n (diode) junction and the series resistance at the base contact.

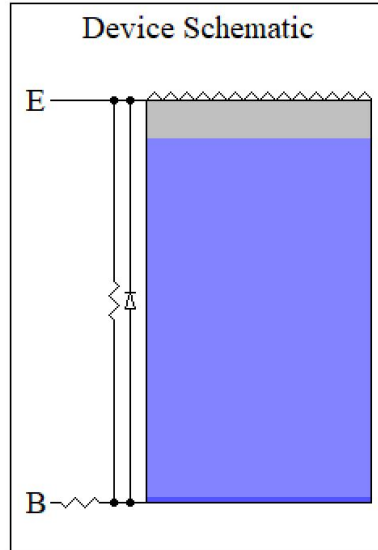


Figure 3.1: PC1D modeling device schematic.

For a start, Table 3.1 shows the input parameters for modeling a four-street and five-busbar (4S-5BB) Al-BSF solar cell fabricated in our lab [20]. The parameters shown in Table 3.1 led to J_{sc} of 38.6 mA/cm^2 , V_{oc} of 643.7 mV , FF of 78.9% and efficiency of 19.6% . This cell was more efficient than average Al-BSF commercial cell of 19.1% efficiency [21]. The 4S-5BB cell had 89 gridlines with narrow width of $< 50 \mu\text{m}$ plus uneven busbars to cut back on total front shading. This led to the metal coverage of only 3.97% and series resistance of $0.739 \Omega \cdot \text{cm}^2$. To account for the antireflective coating of 4% with silicon nitride atop a textured surface [22], a total front reflectance of 7.5% was used. A minority carrier lifetime of 500 ns was used [23], with front surface recombination velocity of 2000 cm/s based on the emitter doping concentration and surface passivation layer [24]. The rear surface recombination velocity of 250 cm/s matched the base resistivity of $2 \Omega \cdot \text{cm}$ and polished wafer with metal coverage [25].

Another object of this thesis work is to explore the possibility of contacting lowly doped emitter ($140 \Omega/\text{sq}$) with low total series resistance, the design then would require a combination of low metal coverage as in the 4S-5BB structure, high minority

Table 3.1: PC1D modeling: device initial parameters

<p>DEVICE Device modified from pvcell.dev Device area: 1 cm^2 Front surface texture depth: 3 um No surface charge Exterior Front Reflectance: 7.5 % Internal optical reflectance enabled Rear surface optically rough Emitter contact enabled Base contact: 0.739Ω Internal conductor: $1.47 \times 10^{-5} S$ Internal diode: $1 \times 10^{-9} A$</p> <p>REGION 1 Thickness: 180 um Material modified from si.mat Carrier mobilities from internal model Dielectric constant: 11.9 Band gap: $1.124 eV$ Intrinsic conc. at 300K: $1 \times 10^{10} \text{ cm}^{-3}$ Refractive index from: Si.inr Absorption coeff. from Si300.abs Free carrier absorption enabled P-type background doping: $5.48 \times 10^{15} \text{ cm}^{-3}$ 1st front diff.: N-type, $6.9 \times 10^{19} \text{ cm}^{-3}$ peak Bulk recombination: $\tau_n = \tau_p = 500 \text{ us}$ Front-surface recombination: S model, $S_n = S_p = 2000 \text{ cm/s}$ Rear-surface recombination: S model, $S_n = S_p = 250 \text{ cm/s}$</p> <p>EXCITATION Excitation modified from on-sun.exc Excitation mode: Transient, 50 timesteps Temperature: $25^\circ C$ Base circuit: Sweep from $-0.8 \text{ to } 0.8 V$ Collector circuit: Zero Primary light source enabled Constant intensity: $0.1 W \text{ cm}^{-2}$ Spectrum from am15g.spc Secondary light source disabled</p> <p>RESULTS Short-circuit Ib: -0.0386 amps Max base power out: 0.0196 watts Open-circuit Vb: 0.6437 volts</p>

carrier lifetime of the bulk material, and low surface recombination velocity on the front since the back side depends on bulk resistivity. Putting these excellent input parameters led to J_{sc} of 42.3 mA/cm^2 , V_{oc} of 704.3 mV , FF of 82.6% and efficiency of 24.6% . This is quite close to the theoretical limit of *Si* solar cell efficiency of 29% . More so, since the total reflectance plays a great role in the optical loss and series resistance in the electrical loss, the model was design to study the impact of these two major parameters on J_{sc} , V_{oc} , FF and efficiency as shown in Figures 3.2a to 3.2d.

In Figure 3.2a and 3.2b, while the total front reflectance (FR) (antireflectance and gridline shadowing) is kept constant for each curve, the series resistivity was varied from 0 to $0.8 \Omega - \text{cm}^2$. It is obvious from Figure 3.2b that the series resistance does not have any impact on V_{oc} but the total reflectance showed a very weak relation with a loss of only 2 mV from 0% to 8% . The short circuit current density on the hand has about 3.5 mA/cm^2 loss when the reflectance was changed from 0% to 8% . However, the series resistance of up to $0.8 \Omega - \text{cm}^2$ did not impact the current density, while the FF is more impacted by the series resistance as seen in Figure 3.2c and has up to 4% loss (absolute) as the resistance increases from 0 to $0.8 \Omega - \text{cm}^2$. Thus, the efficiency is strongly dependent on the series resistance, since efficiency is a multiplication of three parameters including the FF . That is why this work is very important, in particular, to reduce the total series resistance to improve the efficiency of the solar cell.

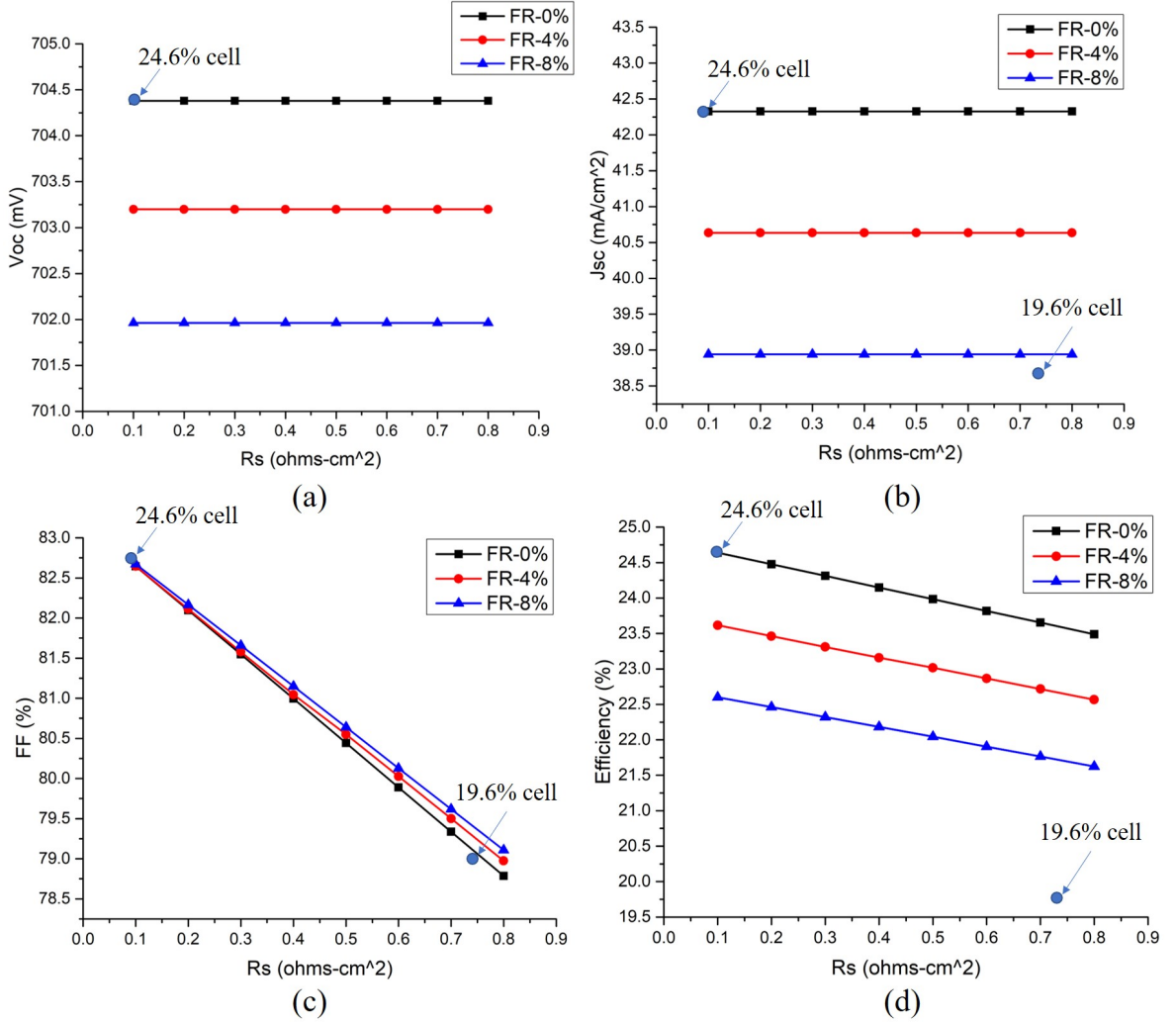
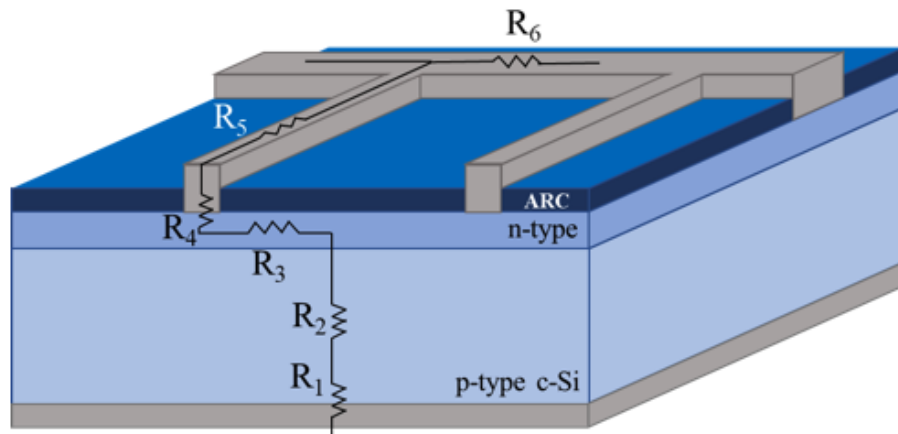


Figure 3.2: Impact of R_s on the (a) V_{oc} , (b) J_{sc} , (c) FF and (d) Efficiency under different FR.

To reduce the R_s , better design of the gridlines is one way. In Figure 3.3, the total series resistance of a solar cell constitutes R_1 to R_6 as defined. Among all the resistance sources, R_1 is the resistance between Al and the bulk Si for an Al-BSF solar cell. R_2 is the bulk resistance based on the Si wafer resistivity. However, R_3 , R_5 and R_6 can be reduced through the gridline design. R_4 is the contact resistance between the gridline and the Si emitter, which has been thought to depend on the emitter surface doping concentration.



- (i) R_1 : metal-semiconductor back contact
- (ii) R_2 : bulk semiconductor
- (iii) R_3 : emitter between two gridlines
- (iv) R_4 : metal-semiconductor contact on gridline
- (v) R_5 : gridline
- (vi) R_6 : busbar

Figure 3.3: Components of series resistance in solar cells.

As predicted by ITRPV [7], lowly doped emitter having $140 \Omega/sq$ sheet resistance has the most potential to improve the solar cell efficiency close to the theoretical limit. Figure 3.4 shows the relationship between the sheet resistance and the peak surface doping concentration of an emitter as modeled by PC1D. It shows the emitter with sheet resistance of $140 \Omega/sq$ has ~ 2 times lower peak surface doping concentration (N_s) than $80 \Omega/sq$ emitter. Based on this, the effect of lowly doped emitter in the solar cell is modeled and shown in Figure 3.5. The lowly doped emitter shows improved V_{oc} and J_{sc} . By increasing the N_s from $4.43 \times 10^{19} cm^{-3}$ to $9.16 \times 10^{19} cm^{-3}$, the efficiency is decreased by $\sim 0.8\%$, while the FF is increased by $\sim 0.4\%$. The overall benefits of applying the lowly doped emitter is due to its better surface passivation with lower emitter recombination and easy to be passivated. Thus, the best cell having a lowly doped emitter with J_{sc} of $42.3 mA/cm^2$, V_{oc} of $704.3 mV$, FF of 82.6% and efficiency of 24.6% can be achieved.

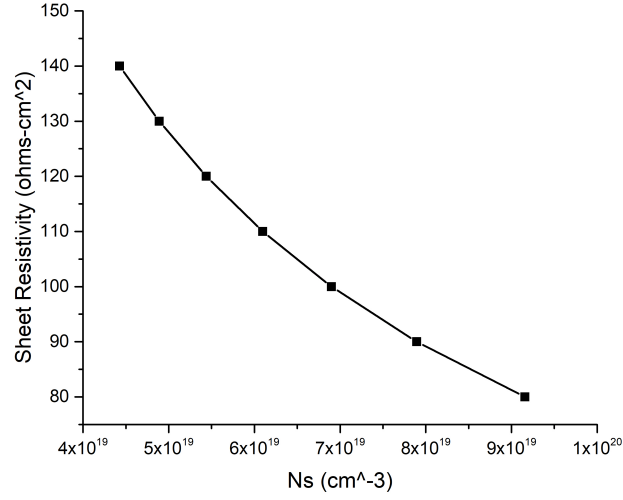


Figure 3.4: The relationship between surface doping concentration and the emitter resistivity.

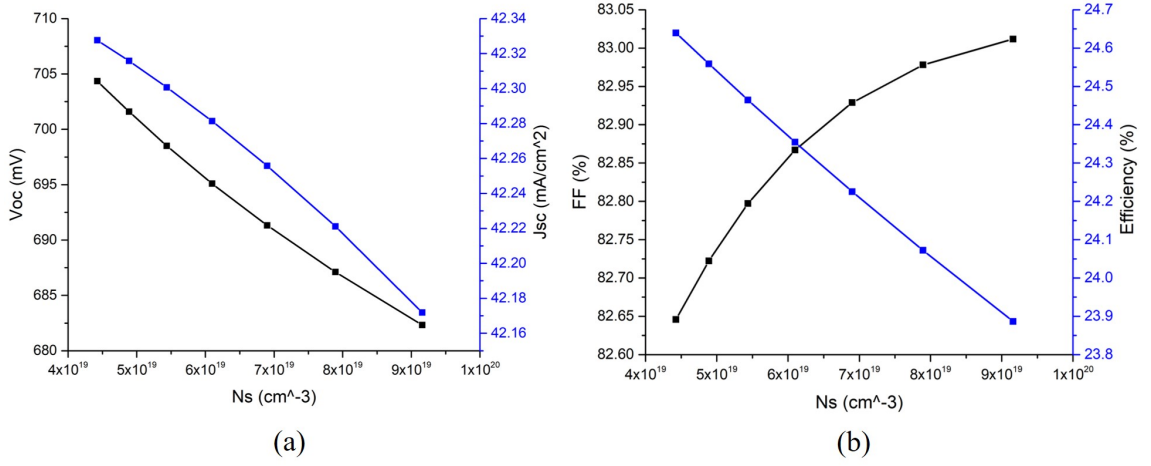


Figure 3.5: Impact of N_s on the (a) V_{oc} and J_{sc} , (b) FF and Efficiency.

However, this modeling is based on the assumption that the overall R_s is constant under different doping concentration and is very low. Actually, the R_s will be changed with doping concentration because the contact resistance, R_4 , is a function of emitter doping concentration. $R_4 = \frac{\rho_c}{l_g \times w_g}$, where ρ_c is the specific contact resistivity, which is proposal to $\frac{1}{\sqrt{N_s}}$, l_g is the gridline length and w_g is the gridline width. Hence, for the same gridline structure, the reduced N_s will increase the R_s by causing higher ρ_c .

In order to reach higher efficiency on lowly doped emitter, R_4 should be kept low. To contact the lowly doped emitter with low specific contact resistivity in a solar cells, it is crucial to understand through microstructure analyses of the interface between the gridline and silicon.

CHAPTER 4: EXPERIMENTAL

To understand the contact mechanism through microstructure analyses, four Ag pastes with different amounts of TeO_2 glass were used to fabricate Al-BSF cells. These cells were based on p-type Czochralski (CZ) monocrystalline silicon substrates with resistivity of $2.0 \Omega \cdot cm$, sheet resistance of $95 \Omega/sq$, thickness of $180 \mu m$ and size of $239 cm^2$. The fabrication process flow is given in Figure 2.9 (section 2.4). Texturing, emitter formation and AR coating were carried out on production line. The blue wafers were screen-printed with full Al contacts on the rear side and dried at $200^\circ C$ for 2 *minutes*, and then the Ag gridlines were printed with four different pastes (A, B, C, D) each, on the front side plus dry. This was followed by co-firing of the contacts in an infrared (IR) belt furnace at peak temperature of $813^\circ C$ with a belt speed of $230 ipm$. The cells were then characterized through I-V measurements to obtain the V_{oc} , J_{sc} , FF and efficiency. Both series and contact resistances were obtained where the contact resistance were obtained through TLM method [26].

To study the microstructure of the front contact interface, which is critical to understand contacting lowly doped emitters, two sets of samples were prepared. One set of samples that were treated in 70% HNO_3 at $80^\circ C$ for 10 *minutes* to remove the Ag gridlines and preserve the underlying glass layer that bonds the gridlines to the silicon surface; and the other set of samples had the Ag gridlines and glass removed by dipping in 2.5% HF at room temperature for 4 *minutes* to remove glass layers after the HNO_3 treatment. The morphology and the components of the microstructures at gridlines/ Si interface were acquired using SEM with EDS (JEOL w/ EDS, Model 6460LV) and Raman spectrometer (HORIBA, XploRaTMPLUS) excited at $532 nm$.

4.1 Electrical Analyses

The electrical properties of the four best cells from each paste are listed in Table 4.1. Cells with paste B and D have similar efficiency of $\sim 20\%$. However, the sample using paste D had the highest fill factor (FF) due to lower contact resistance. The efficiency and the FF of sample C are lower than both samples B and D, which could be due to other factors including high contact resistance. The sample with paste A has the highest contact and series resistances, which was strong enough to impact the open-circuit voltage (V_{oc}) and short-circuit current density (J_{sc}). Hence, the sample with paste A exhibited the lowest FF and the efficiency. Since samples with pastes B, C and D had very close output characteristics, the microstructure analyses was carried out on A the worst and D the best cells.

Table 4.1: Electrical properties of the four samples made by different pastes [27]

Ag Paste	V_{oc} (mV)	J_{sc} (mA \cdot cm $^{-2}$)	FF (%)	Efficiency (%)	ρ_c (m Ω cm 2)	ρ_s (m Ω cm 2)
A	634.30	38.68	46.53	11.42	0.83	11.66
B	641.70	39.58	78.96	20.05	0.44	0.73
C	641.82	39.50	78.34	19.85	0.39	0.83
D	642.08	39.40	79.15	20.03	0.31	0.69

4.2 Micro-Structure Analyses

4.2.1 SEM and EDS

Figure 4.1 shows the SEM - backscattered electron composition (BEC) images of the sample made from paste A. Figures 4.1a and 4.1b show the interface of the Ag gridline and Si before the removal of the Ag gridline. From this image, a re-crystallized glass in the Ag gridline with $\sim 1 \mu m$ size can be observed. This glass layer is non-uniform and thick. This could have been due to poor dispersion of the glass particles in the paste that led to non-uniform wetting and etching of ARC. Figures 4.1c and 4.1d depict the interface underneath the Ag gridline/ Si without the

Ag gridline. This image shows some glass remains on the surface but no metal alloys in the glass, which is necessary to conduct the carriers from *Si* to the *Ag* gridlines. This explains why the contact resistance for this cell was so high. Figures 4.1e and 4.1f, show the interface after the *HF* treatment, which completely removed the glass and the *Ag* gridlines. The images exhibit *Si* surface showing the pyramids from texturing and few spaced metal crystallites.

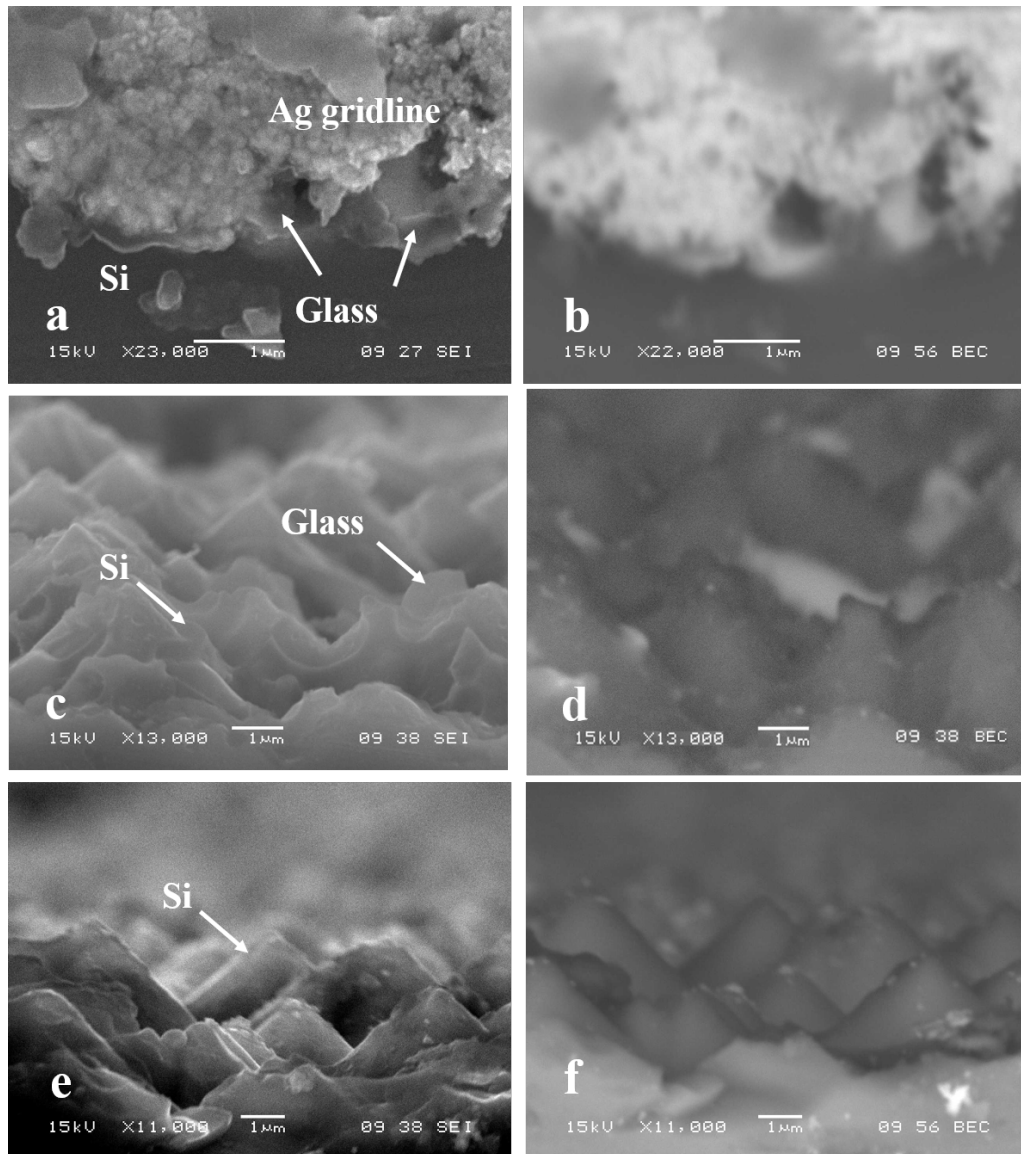


Figure 4.1: SEM cross-section images of A, (a-b) before acid treatment, (c-d) after *Ag* gridline removal; (e-f) after interface glass removal [27].

On the other hand, Figures 4.2a and 4.2b show the *Ag/Si* interface for cell based on paste D with the *Ag* gridlines. The images reveal some *Ag* crystallites regrown in the bulk *Si*. The glass dispersion in this paste uniformly wetted, etched the ARC and formed thinner glass layer, which in turn led to lower contact resistance. This behavior could be due to glass frits in paste D having a lower transition temperature (T_g) than that in paste A. This result is supported by the works [28, 29], which showed that the complete etching of the ARC during high temperature contact firing is a function of the glass frits transition temperature. The glass with higher T_g requires, higher firing temperature. Thus, paste D had glass frit with low T_g , that is why the interface showed uniform glass layer after cooling as depicted in the SEM.

Figures 4.2c and 4.2d show the image of the interface underneath the removed gridline. It can be seen the textured surface with the pyramids covered by the glass layer. The BEC image reveals that there are many metal colloids and metal crystallites with various sizes at the interface. In order to specify the location of the metal colloids and crystallites, the glass layer was removed, which led to Figures 4.2e and 4.2f. As depicted in Figures 4.2e and 4.2f, there have some metal crystallites grown into *Si* surface, during the contact firing, while no metal colloids found at the *Si* surface once the glass was removed. This leads to the conclusion that the metal colloids are mostly in the glass which bonds the *Ag* gridlines to *Si*. This observation indicates that the conductivity of the glass underneath the contact is increased due to the presence of the metal colloids and hence a decrease in contact resistance. Therefore, while the *Ag* crystallites conduct carriers out of *Si*, the metal colloids aid these carriers to be collected at the *Ag* gridlines.

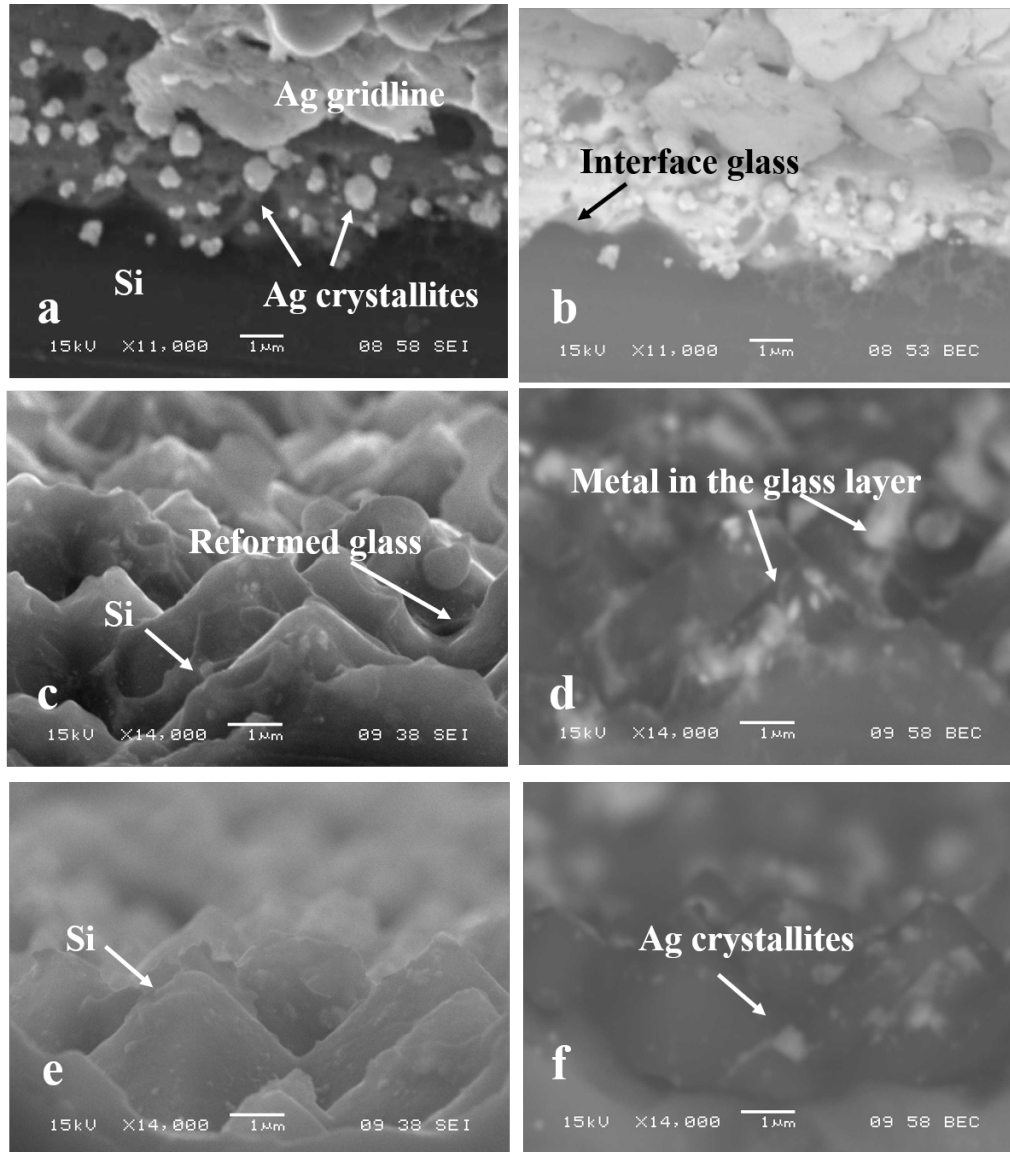


Figure 4.2: SEM cross-section images of sample D, (a-b) before acid treatment, (c-d) after *Ag* gridline removal; (e-f) after interface glass removal [27].

From the analyses of the samples with the two pastes, it is evident that the metal colloids in the interface glass layer play a major role in the value of the ρ_c . The higher the amount of metal colloids in the glass layer, the lower ρ_c , and ρ_s , and hence the increase in the FF and the efficiency. The sample with paste A had thick glass layer at the interface but with very little amount of metal colloids in addition to fewer *Ag* crystallites in *Si*. The low ρ_c for the sample with paste D is mainly due to the large

amount of metal colloids in the glass layer in addition to the more *Ag* crystallites in *Si*. This is quite in agreement with the findings of Hoenig et al [30], where the silver colloids formed in the interface glass layer was said to cause a dramatic increase in the conductivity of the glass layer leading to low ρ_s .

Based on the micro-structure of *Ag/Si* contact, the current transport paths from *Si* emitter to *Ag* gridlines include [31, 32]:

- (a) through *Ag* crystallites direct contact with *Si* emitter;
- (b) tunneling through an ultrathin glass layer;
- (c) through *Ag* nanoparticle assisted tunneling;

The 4th path could be attributed to the metal colloids or "nano-*Ag* colloids" [27] that increase the conductivity of the glass that bonds *Ag* gridlines to silicon based on this thesis work. This agrees with the proposed "nano-colloid assisted tunneling" in reference [33].

Further analysis on sample with paste D was carried out to ascertain the elemental composition through Energy Dispersive X-ray Spectroscopy (*EDS*). Figure 4.3a shows an *EDS* of the glass layer underneath the metal contact with the associated elemental composition of the metal colloids. Elements such as *Al*, *Pb*, *Bi*, *Ag* and *Te*, and *Bi* were revealed. It should be noted that these elements are glass composite instead of the colloids. However, after the interface glass removal as depicted in Figure 4.3b, there is no evidence of *Pb*, *Te* or *Bi*. This means that the colloids consist mainly the alloy of *Pb*, *Ag* and *Te*, while the crystallites is mainly *Ag* metal.

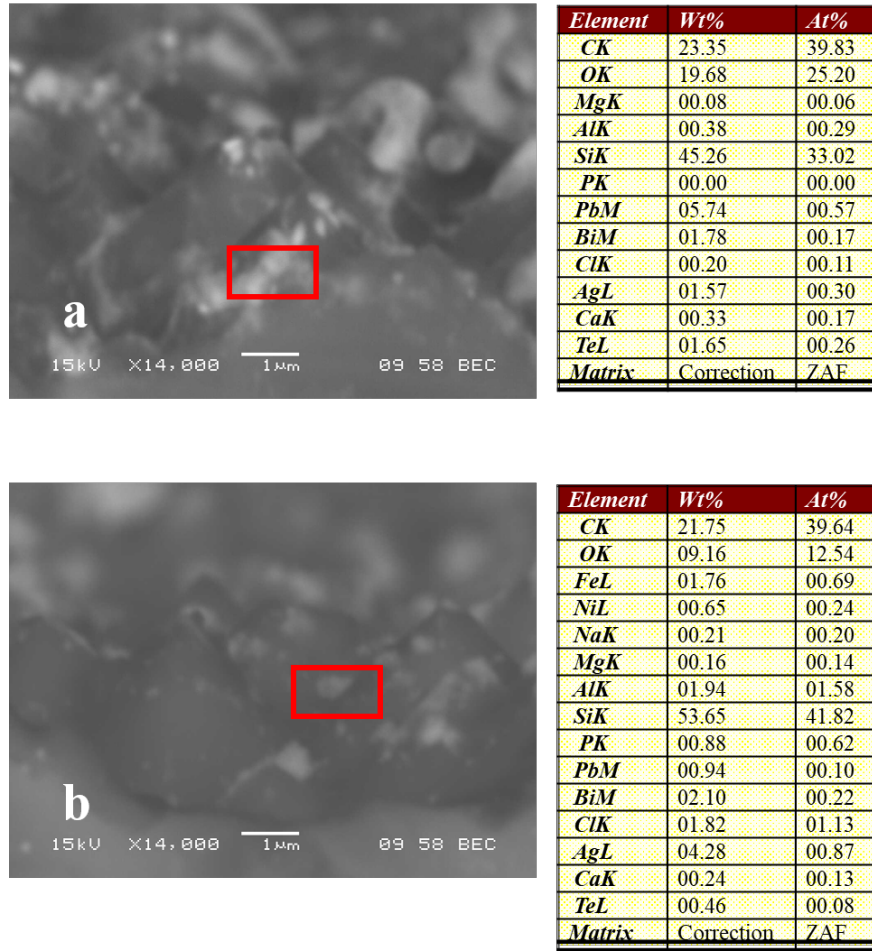


Figure 4.3: EDS analyses of selected area on sample D (a) after *Ag* gridline removal; (b) after interface glass removal [27].

4.2.2 Raman Study

To confirm the metal colloids composition, the Raman spectrometer was used and the spectroscopy of samples with paste A and D is shown in Figure 4.4. According to the references, Ag_2Te has peaks at 80 cm^{-1} [34], 119 cm^{-1} and 145 cm^{-1} [35]. The peaks around 396 cm^{-1} and 641 cm^{-1} are due to the bending vibration in TeO_2 . The 675 cm^{-1} peak corresponds to symmetrical stretching of $Te - O$ [35, 36]. But $PbTe$ has peaks at 119 cm^{-1} , 183 cm^{-1} and 366 cm^{-1} . The strong peak at 520 cm^{-1} comes from *Si* substrate. Sample with paste A does not have peaks at 76 cm^{-1} , 119 cm^{-1} , 145 cm^{-1} , 183 cm^{-1} , $363 - 401\text{ cm}^{-1}$, 520 cm^{-1} and 660 cm^{-1} , which have to do with

the Ag_2Te and $PbTe$. Thus, the Raman spectra confirms the formation of Ag_2Te and $PbTe$ in sample with paste D instead. The fact that after glass removal, the Ag_2Te and $PbTe$ peaks were absent confirms that Ag_2Te and $PbTe$ are the property of the glass and not the Si emitter. This result further buttresses the EDS results in Figure 4.4, which shows that after Ag gridline removal, the ratio of the $At\%$ of Te , Pb and Ag was around 1.0: 2.2: 1.2. This strongly suggests the formation of the alloys of Ag_2Te and $PbTe$ in the colloids. In Figure 4.4, after glass layer removal, the ratio between Te , Pb and Ag was 1.0: 1.3: 10.9 which indicates the metal crystallite is mainly Ag metal.

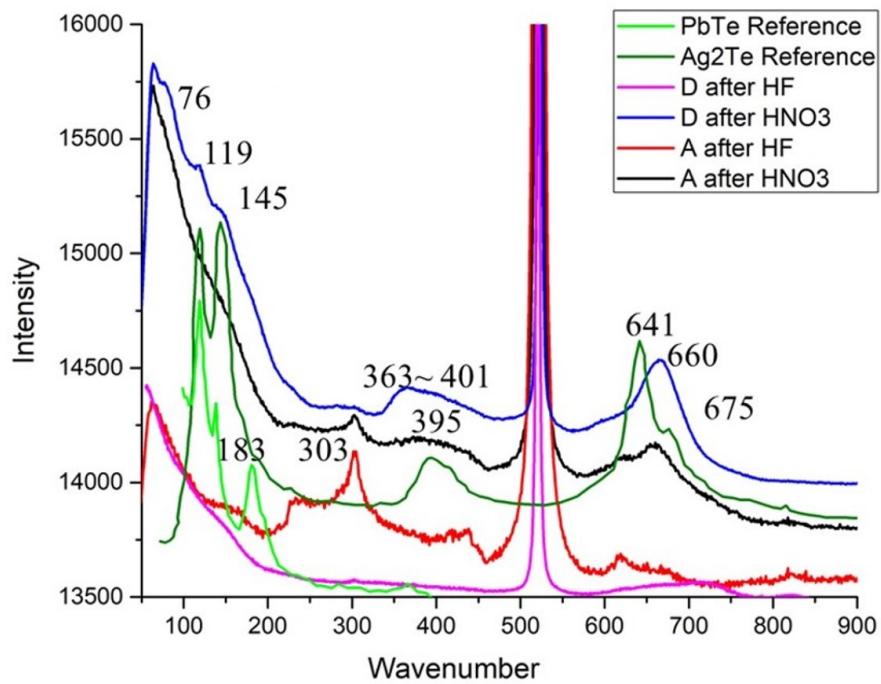


Figure 4.4: Raman spectroscopy of sample A, D after HNO_3 and HF treatment and Ag_2Te [35], $PbTe$ [37].

CHAPTER 5: CONCLUSIONS

Through the microstructure analysis of the *Ag* gridline /*Si* interface with the SEM, EDS and Raman Spectrometer, it was evident that the glass layer at this interface is as important as the *Ag* crystallites embedded in the Si emitter after the contact formation step. SEM showed a thick or thin glass layer at the interface depending on the glass transition temperature (T_g) of the glass frit. The thick or thin glass layer dictates the contact resistance value and hence the total series resistance and FF . The SEM also revealed that, if the underlying ARC is not uniformly etched, the glass layer will not be uniform and the *Ag* crystallites embedded in the *Si* emitter will be fewer compared to the uniformly etched counterpart. The EDS revealed *Pb*, *Al*, *Ag*, *Te* and *Bi* elements in the glass, which was confirmed by the Raman Spectroscopy. These elements were absent after the glass was etched off, except *Ag* was found in the Si emitter. This confirmed that the low contact resistance exhibited by the best sample is due to the formation of alloys of *Pb* and *Te* as confirmed by Raman spectra. The different peaks at various positions in the Raman Spectra were consistent with compounds of *Te* and *Pb*. Thus, the thesis work has concluded that the presence of these alloys of *Pb* and *Te* increases the conductivity of the glass layer at the *Ag/Si* interface and enhance the collection of carriers with less $I^2 \cdot R$ loss.

CHAPTER 6: FUTURE WORK

To understand the current transport mechanism through the Ag_2Te and $PbTe$ colloids in the interface glass layer, the distribution of these metal colloids should be studied. In addition, it is necessary to use transmission electron microscopy (TEM) to analyze the thickness of the metal colloids and the conducting AFM ($C - AFM$) to study the nature of the colloids conduction through $I - V$ curves. Based on the $I - V$ measurement and the conductivity of the colloids, the role of these colloids in the current transport mechanism will be revealed. To further explain the contact mechanism, the band structure of the Ag /semi-metal colloids/ Si emitter contact should be calculated in addition to resonant tunneling probability

REFERENCES

- [1] C. S. Watson, N. J. White, J. A. Church, M. A. King, R. J. Burgette, and B. Legresy, “Unabated global mean sea-level rise over the satellite altimeter era,” *Nature Climate Change*, vol. 5, no. 6, p. 565, 2015.
- [2] J. Hansen, R. Ruedy, M. Sato, and K. Lo, “Global surface temperature change,” *Reviews of Geophysics*, vol. 48, no. 4, 2010.
- [3] “International energy outlook,” tech. rep., USDOE Energy Information Administration (EIA), Washington, DC (United States). Office of Energy Analysis, 2017.
- [4] J. Conti, P. Holtberg, J. Diefenderfer, A. LaRose, J. T. Turnure, and L. Westfall, “International energy outlook 2016 with projections to 2040,” tech. rep., USDOE Energy Information Administration (EIA), Washington, DC (United States). Office of Energy Analysis, 2016.
- [5] U. E. I. Administration, *Annual Energy Outlook 2017 with projections to 2050*. Independent Publishing Platform, 2017.
- [6] “Nrel efficiency chart.” <https://www.nrel.gov/pv/assets/images/efficiency-chart.png>. Accessed: 2018-04-06.
- [7] “Itrpv report 2018 edition.” <http://www.itrpv.net/Reports/Downloads/>. Accessed: 2018-08-06.
- [8] D. M. Chapin, C. Fuller, and G. Pearson, “A new silicon p-n junction photocell for converting solar radiation into electrical power,” *Journal of Applied Physics*, vol. 25, no. 5, pp. 676–677, 1954.
- [9] “Understanding the p-n junction.” http://www2.pv.unsw.edu.au/nsite-files/pdfs/UNSW_Understanding_the_p-n_Junction.pdf. Accessed: 2018-04-05.
- [10] “Light generated current.” <http://pvcadrom.pveducation.org/CELLOPER/ILIGHT.htm>. Accessed: 2018-03-30.
- [11] M. M. Hilali, K. Nakayashiki, A. Ebong, and A. Rohatgi, “High-efficiency (19%) screen-printed textured cells on low-resistivity float-zone silicon with high sheet-resistance emitters,” *Progress in Photovoltaics: Research and Applications*, vol. 14, no. 2, pp. 135–144, 2006.
- [12] Y.-C. Hsu, *Investigation of Abnormal Behavior of Light Induced Degradation (LID) In Cost-Effective Industrial Aluminum Back Surface Field (AL-BSF) Silicon Solar Cells*. PhD thesis, The University of North Carolina at Charlotte, 2017.
- [13] J. Nelson, *The physics of solar cells*. World Scientific Publishing Company, 2003.

- [14] “Quantum efficiency.” https://en.wikipedia.org/wiki/Quantum_efficiency. Accessed: 2018-03-30.
- [15] P. S. Priambodo, D. Sukoco, W. Purnomo, H. Sudiby, and D. Hartanto, “Electric energy management and engineering in solar cell system,” in *Solar Cells-Research and Application Perspectives*, InTech, 2013.
- [16] K. Yoshikawa, W. Yoshida, T. Irie, H. Kawasaki, K. Konishi, H. Ishibashi, T. Asatani, D. Adachi, M. Kanematsu, H. Uzu, *et al.*, “Exceeding conversion efficiency of 26% by heterojunction interdigitated back contact solar cell with thin film si technology,” *Solar Energy Materials and Solar Cells*, vol. 173, pp. 37–42, 2017.
- [17] K. H. Kim, C. S. Park, J. D. Lee, J. Y. Lim, J. M. Yeon, I. H. Kim, E. J. Lee, and Y. H. Cho, “Record high efficiency of screen-printed silicon aluminum back surface field solar cell: 20.29%,” *Japanese Journal of Applied Physics*, vol. 56, no. 8S2, p. 08MB25, 2017.
- [18] W. Deng, F. Ye, R. Liu, Y. Li, H. Chen, Z. Xiong, Y. Yang, Y. Chen, Y. Wang, P. P. Altermatt, *et al.*, “22.61% efficient fully screen printed perc solar cell,” in *Proc. 44th IEEE PVSC*, 2017.
- [19] D. A. Clugston and P. A. Basore, “Pc1d version 5: 32-bit solar cell modeling on personal computers,” in *Conference Record of the Twenty Sixth IEEE Photovoltaic Specialists Conference-1997*, pp. 207–210, IEEE, 1997.
- [20] A. Ebong, N. Chen, V. Unsur, A. Chowdhury, and B. Damiani, “Innovative front grid design, four-streets and five-busbars (4s-5bb), for high efficiency industrial al-bsf silicon solar cell,” *IEEE Electron Device Letters*, vol. 37, no. 4, pp. 459–462, 2016.
- [21] S. Gatz, H. Hannebauer, R. Hesse, F. Werner, A. Schmidt, T. Dullweber, J. Schmidt, K. Bothe, and R. Brendel, “19.4%-efficient large-area fully screen-printed silicon solar cells,” *physica status solidi (RRL)–Rapid Research Letters*, vol. 5, no. 4, pp. 147–149, 2011.
- [22] G. Ayvazyan, R. Barseghyan, and S. Minasyan, “Optimization of surface reflectance for silicon solar cells,” *E3S Web of Conferences*, vol. 69, p. 01008, 01 2018.
- [23] S. W. Glunz, S. Rein, W. Warta, J. Knobloch, and W. Wettling, “Degradation of carrier lifetime in cz silicon solar cells,” *Solar energy materials and solar cells*, vol. 65, no. 1-4, pp. 219–229, 2001.
- [24] M. Kerr, J. Schmidt, A. Cuevas, and J. Bultman, “Surface recombination velocity of phosphorus-diffused silicon solar cell emitters passivated with plasma enhanced chemical vapor deposited silicon nitride and thermal silicon oxide,” *Journal of Applied Physics*, vol. 89, no. 7, pp. 3821–3826, 2001.

- [25] T. Lauinger, J. Schmidt, A. G. Aberle, and R. Hezel, "Record low surface recombination velocities on 1 ω cm p-silicon using remote plasma silicon nitride passivation," *Applied Physics Letters*, vol. 68, no. 9, pp. 1232–1234, 1996.
- [26] P. Vinod, "Specific contact resistance measurements of the screen-printed ag thick film contacts in the silicon solar cells by three-point probe methodology and tlm method," *Journal of Materials Science: Materials in Electronics*, vol. 22, no. 9, pp. 1248–1257, 2011.
- [27] K. Ren, V. Unsur, A. Chowdhury, Y. Zhang, and A. Ebong, "The impact of tellurite glass on contact resistance of the fire through dielectric (ftd) c-si solar cell with lightly doped emitter," in *2018 IEEE 7th World Conference on Photovoltaic Energy Conversion (WCPEC)(A Joint Conference of 45th IEEE PVSC, 28th PVSEC & 34th EU PVSEC)*, pp. 1051–1054, IEEE, 2018.
- [28] X.-X. Pi, X.-H. Cao, Z.-X. Fu, L. Zhang, P.-D. Han, L.-X. Wang, and Q.-T. Zhang, "Application of te-based glass in silicon solar cells," *Acta Metallurgica Sinica (English Letters)*, vol. 28, no. 2, pp. 223–229, 2015.
- [29] J. Qin, S. Bai, W. Zhang, Z. Liu, and H. Wang, "Effects of organic medium on rheological properties of silver pastes for crystalline silicon solar cells," *Circuit World*, vol. 42, no. 2, pp. 77–83, 2016.
- [30] R. Hoenig, M. Duerrschnabel, W. van Mierlo, Z. Aabdin, J. Bernhard, J. Biskupek, O. Eibl, U. Kaiser, J. Wilde, F. Clement, *et al.*, "The nature of screen printed front side silver contacts-results of the project mikrosol," *Energy Procedia*, vol. 43, pp. 27–36, 2013.
- [31] G. Grupp, D. Huljic, R. Preu, G. Willeke, and J. Luther, "Peak firing temperature dependence of the microstructure of ag thick-film contacts on silicon solar cells—a detailed afm study of the interface," *Proc. 20th EC PVSEC*, 2005.
- [32] E. Cabrera, S. Olibet, J. Glatz-Reichenbach, R. Kopecek, D. Reinke, and G. Schubert, "Experimental evidence of direct contact formation for the current transport in silver thick film metallized silicon emitters," *Journal of Applied Physics*, vol. 110, no. 11, p. 114511, 2011.
- [33] H. Mäckel and P. P. Altermatt, "Current transport through lead–borosilicate interfacial glass layers at the screen–printed silver–silicon front contact," *IEEE Journal of Photovoltaics*, vol. 5, no. 4, pp. 1034–1046, 2015.
- [34] T. Milenov, T. Tenev, I. Miloushev, G. Avdeev, C. Luo, and W. Chou, "Preliminary studies of the raman spectra of ag_2te and ag_5te_3 ," *Optical and Quantum Electronics*, vol. 46, no. 4, pp. 573–580, 2014.
- [35] A. Qin, Y. Fang, P. Tao, J. Zhang, and C. Su, "Silver telluride nanotubes prepared by the hydrothermal method," *Inorganic chemistry*, vol. 46, no. 18, pp. 7403–7409, 2007.

- [36] C. Kaito, N. Nakamura, K. Teranishi, S. Sekimoto, and M. Shiojiri, “High resolution electron microscopic studies of the polymorphic transformation and crystal structures of low-temperature ag_2se phases,” *physica status solidi (a)*, vol. 71, no. 1, pp. 109–119, 1982.
- [37] B. Zhang, C. Cai, H. Zhu, F. Wu, Z. Ye, Y. Chen, R. Li, W. Kong, and H. Wu, “Phonon blocking by two dimensional electron gas in polar cdte/pbte heterojunctions,” *Applied Physics Letters*, vol. 104, no. 16, p. 161601, 2014.